



In flow acoustic characterisation of a 2D active liner with local and non local strategies.



K. Billon^{a,*}, E. De Bono^a, M. Perez^a, E. Salze^b, G. Matten^c, M. Gillet^c, M. Ouisse^c, M. Volery^d, H. Lissek^d, J. Mardjono^e, M. Collet^a

^a Univ. Lyon, École Centrale de Lyon, LTDS UMR 5513, F-69134 Ecully, France

^b Univ. Lyon, École Centrale de Lyon, LMFA UMR 5509, F-69134 Ecully, France

^c Univ. Bourgogne Franche-Comté, FEMTO-ST Institute, CNRS/UFC/ENSMM/UTBM, Department of Applied Mechanics, 24 rue de l'Épitaphe, F-25000 Besançon, France

^d Signal Processing Laboratory LTS2, Ecole Polytechnique Fédérale de Lausanne, Station 11, CH-1015 Lausanne, Switzerland

^e Safran Aircraft Engines, F-75015, Paris, France

ARTICLE INFO

Article history:

Received 21 July 2021

Received in revised form 6 December 2021

Accepted 19 January 2022

Keywords:

Active liner

Electroacoustic absorber

Impedance control

Active sound absorption

Lined duct

ABSTRACT

The design and the grazing flow aeroacoustical characterization of a 2D active liner based on an array of electroacoustic absorbers are presented in this paper. The strategy stands on a pressure-based, current-driven digital architecture for impedance control with both local and non local architectures. A wind tunnel test rig is used for the in-flow experimental validation. The stability and robustness of the whole system are investigated as a function of flow velocity showing the efficiency of the proposed approach. The air flow slightly reduces the efficiency while maintaining the adaptability and the stability, and better performances are obtained with the non local control strategy.

© 2022 The Authors. Published by Elsevier Ltd. This is an open access article under the CC BY-NC-ND license (<http://creativecommons.org/licenses/by-nc-nd/4.0/>).

1. Introduction

Reducing noise emissions is one of the main design targets driving the development of new aircraft engines. It is therefore a key priority for the competitiveness of our industry especially for developing new technological solutions allowing improvement of engine efficiency and gas emission decrease. For aerospace industry, Ultra-high bypass ratios (UHBR) turbofan engines are expected to equip the next generation of aircrafts to maximise their performances, resulting in an increase of the low frequency contents of the noise generated by these engines compared to existing technologies. Also, with a thinner nacelle, acoustic liners performance is expected to drop at low frequencies, and with a shorter nacelle, less surface area will be available for acoustic treatments. UHBR engine technologies then represent significant challenges for the design of next-generation acoustic treatments. In order to meet the required noise performance at engine level, novel acoustic treatments should achieve significant noise reduction with limited surface, breaking quarter-wavelength rule. This paper presents new results obtained with innovative acoustic treatments concepts

based on the synthesis of local and non local impedance by using electroactive loudspeakers and microphones.

Indeed, the lining specifications given by aircraft manufacturers are usually defined in terms of acoustic impedance (resistance and reactance) which depends on the frequency, the section of the duct, the boundary conditions, the geometry of the liner and the air flow speed. Sound attenuation optimisation in a lined duct has been deeply studied by Cremer for the least attenuated mode with no fluid flow [1,2] and with uniform flow by Tester and al [3]. Acoustic treatments currently used in aircraft nacelles are passive such as a Single Degree of Freedom (SDOF) liner which is made of closed honeycomb cavities with a perforated plate or wiremesh. The acoustic performance of these liners are directly linked to their geometries [4,5]. The impedance of these passive liners is defined for a specific engine regime resulting in strong noise attenuation at the corresponding frequency, however it cannot be modified with the engine speed to adapt to other flight phases like landing or take-off. Moreover, UHBR Technologies, with small thickness and treated surface area limit efficiency of passive systems. The liners conventionally used are also based on quarter-wave resonators or Helmholtz resonators are not suitable for low-frequency treatments which require a large thickness.

* Corresponding author.

E-mail address: kevin.billon@ec-lyon.fr (K. Billon).

Active Liners can outperform conventional acoustic treatments and adapt their performances in real-time to varying engine speeds but need an external energy source at least for computing its behaviour via dedicated electronics. Several strategies have been proposed in the literature to extend the efficiency or tenability of a acoustic resonators: adaptive SDOF with tunable Helmholtz resonators in [6–11], Double-Degree-Of-Freedom (DDOF) [12] or Multi-Degree-Of-Freedom (MDOFs) [13,14]. The acoustical impedance can also be tuned by using resonator elements in parallel instead in series [15] or by scattering or redistributing the energy with adaptive Helmholtz based liner to maximize the effectiveness of a neighbour passive treatment [16]. Instead of varying the Helmholtz resonators geometries, the Active Noise Control (ANC) can provide an interesting alternative thanks to electromechanical actuators and sensors. The pioneers works of Olson [17] were based on electronic sound absorbers with a loudspeaker and a nearby microphone in a negative feedback loop. A few decades later, an "active equivalent of a quarter wavelength resonator" was achieved through a hybrid passive-active technique [18]. This strategy was extended by [19] to liner applications. This hybrid passive/active absorber has been directly used to achieve tonal noise reduction in flow ducts in normal and grazing incidence, see [20].

Recent works using electroacoustic absorber have shown its efficiency for damping duct modes by using shunted loudspeakers [21,22], direct feedback [23,24], or by using sensorless control of the loudspeaker impedance [25]. The main advantage of the electrical shunting strategy is to guarantee acoustic passivity (and therefore stability [26]) as the acoustic energy is transferred through the loudspeaker diaphragm vibration, to the electrical passive shunted circuit and is finally dissipated into heat. The sensorless variant [25] of the electroacoustic absorber (EA) suffers from the difficulty in the electrical dynamics modelling. Instead, the main drawback of the direct impedance control proposed by Boulandet et al. [24] was the need of an additional sensor for retrieving the speaker velocity. The use of a voltage source to drive the speaker vibration was anyway still an issue as the uncertainties in the electrical dynamics were inevitably involved. The quasi-collocation of speaker (actuator) and microphone (sensor), along with the use a current-driven architecture, allowed to get rid of the electrical dynamics model. The control law proposed by Rivet et al. [27] is based upon the direct inversion of the passive mechanical dynamics of the loudspeaker. This pressure-based current-drive control architecture has been applied to the design of an active lining concept based on an arrangement of electroacoustic absorbers, achieving broadband noise reduction for aircraft engine nacelles applications under grazing flow [28]. A local reacting liner can be defined as acoustically passive if the normal absorption coefficient is positive for all frequencies. Without flow, passivity is a sufficient condition for stability [26]. Stability issues are also observed with digital control. The stability of the digital control is also limited due to its inherent time delay [29]. Indeed, the electroacoustic absorber tends to lose its acoustical passivity at higher frequencies. In order to restore the high-frequency passivity, a thin layer of porous material can be placed in front of the loudspeaker as proposed in [29]. In case of air-flow, the stability is more delicate, as it involves the liner interaction with the boundary layer [30].

In the case of a non-local reacting liner, the interface behaviour cannot only be described by a classical local impedance but also by spatial derivative terms associated to specific boundary waves propagation. In the case considered in this paper, the controlled liner uses a unidirectional non-local behaviour as proposed by [31,32] which interacts with the incoming acoustic flow to cancel propagation in one direction and not in the opposite one, while a part of the acoustic energy is also absorbed. This boundary control

strategy can be named advective impedance control. The application of this boundary condition in an acoustic waveguide produces significant results which can out-perform those obtained with local strategies.

This paper presents an acoustic characterisation of a 2D active liner based on an array of electroacoustic absorbers. The control law is implemented by pressure-based, current-driven digital architecture for impedance control as designed by Rivet [27]. Both local and non-local control strategies are experimentally validated without and with air flow. This paper is organised as follow: In Section 2, the active impedance is described in general. In Section 3, some reminders are given about the implementation of the control strategies and the spatial discretization of the implemented active liner is presented. In Section 4, the test bench facility is introduced. In Section 5, the experimental results without and with flow are presented with local and non-local strategies. Finally, in Section 6, an impedance eduction method with a numerical model is used to identify the effective surface impedance of the active liner based on experimental data.

2. Active impedance strategies

This section presents the active impedance implemented in a lined duct as generally presented in Fig. 1. A locally reacting liner can be described by its targeted impedance:

$$Z_{at} = \frac{p}{v_n}, \quad (1)$$

where v_n is the normal acoustic particle velocity of the surface (S) and p the sound pressure at the surface. Terms targeted impedance will be used in the following because model inversion is used to achieved the target acoustic velocity producing the desired and optimal impedance value. In order to create a non-locally reacting liner, an additional term is added in the Robin boundary condition:

$$Z_{at} \left[\frac{\partial v_n}{\partial t} \right] = \frac{\partial p}{\partial t} - c_a \frac{\partial p}{\partial x}, \quad (2)$$

where c_a represents the transport speed of the advection condition. If $c_a = 0$, the locally reacting behaviour is retrieved (Eq. 1). This boundary condition can be implemented by using a spatial discretization of the derivative term through an array of electroacoustic transducers [31]. Local and non-local control strategies are used in this paper.

3. Implementation of the control strategies - Spatial discretization

3.1. Electroacoustic transducers

The active liner is made of an array of unit cells. Each unit cell is composed of an actuator (a loudspeaker), the four microphones and a control card for the computation of the localized or distributed (non-localized) control (Fig. 2). For the local implementation, the loudspeaker membrane is driven as a function of the collocated parietal pressure estimated by the mean pressure

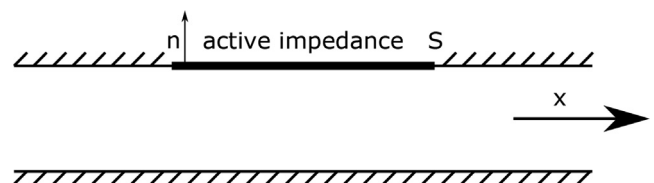


Fig. 1. Scheme of the duct.

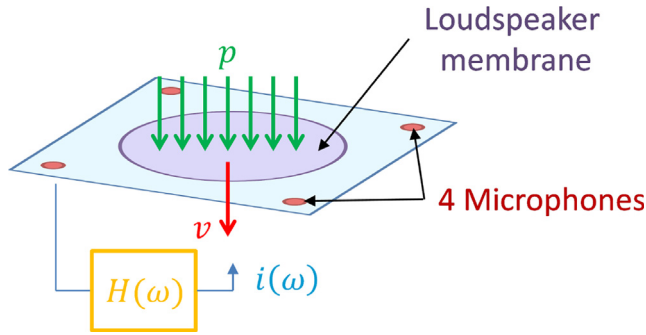


Fig. 2. Schema of the cell control.

measured by the the four microphones. The non-local implementation introduces a term depending on spatial differentiation of two sets of pressure measurements as explained below.

3.2. Local control strategy

The pressure-based, current-driven digital architecture for impedance control is fully explained in [27].

The electromechanical equation driving the loudspeaker in the SDOF piston mode can be written as

$$Z_m(s)v_n(s) = S_d p(s) - Bl i(s), \quad (3)$$

where s stands for the Laplace variable, $v_n(s)$ is the membrane normal velocity of the loudspeaker, $p(s)$ the parietal sound pressure, S_d the equivalent piston area, Bl the force factor of the moving coil and $i(s)$ is the coil electrical current. The mechanical impedance of the SDOF loudspeaker model in open circuit (Z_m) is expressed as:

$$Z_m(s) = sM + R + \frac{1}{sC}, \quad (4)$$

where M , R and C are respectively the mass, resistance and compliance of the SDOF loudspeaker model.

The transfer function (local control) between the pressure measurement and the imposed current for realizing the targeted impedance Z_{at} at the loudspeaker membrane is defined as:

$$H_{loc}(s) = \frac{i(s)}{p(s)} = \frac{1}{Bl} \left(S_d - \frac{Z_m(s)}{Z_{at}(s)} \right), \quad (5)$$

where Z_{at} is the target impedance that can be written as:

$$Z_{at}(s) = \frac{p(s)}{v_n(s)} = \mu_1 \frac{sM}{S_d} + R_{at} + \mu_2 \frac{1}{sCS_d}, \quad (6)$$

with μ_1 and μ_2 are two tunable coefficients representing respectively the reductions of mass and stiffness of the controlled loudspeaker. R_{at} is the target acoustic resistance to be achieved at the controlled loudspeaker resonance.

3.3. Non-local control strategy

The non-local control implementation is summarized below (see details in [31,32]). Using Eq. 2, the velocity can be written in the Laplace domain as:

$$v_n(s) = \frac{1}{Z_{at}} p(s) - \frac{c_a}{Z_{at}s} \frac{\partial p(s, \mathbf{x})}{\partial \mathbf{x}}. \quad (7)$$

The velocity expression (Eq. 7) for the non-local control can be included in the Eq. 3:

$$Z_m(s) \left[\frac{1}{Z_{at}} p(s) - \frac{c_a}{Z_{at}s} \frac{\partial p(s, \mathbf{x})}{\partial \mathbf{x}} \right] = S_d p(s) - Bl i(s), \quad (8)$$

then,

$$Bl i(s) = \left[S_d - \frac{Z_m(s)}{Z_{at}} \right] p(s) + \left[\frac{Z_m(s)c_a}{Z_{at}s} \right] \frac{\partial p(s, \mathbf{x})}{\partial \mathbf{x}}, \quad (9)$$

after formatting the previous expression,

$$i(s) = \frac{1}{Bl} \left[S_d - \frac{Z_m(s)}{Z_{at}} \right] p(s) + \left[\frac{Z_m(s)c_a}{Bl Z_{at}s} \right] \frac{\partial p(s, \mathbf{x})}{\partial \mathbf{x}}. \quad (10)$$

The current in order to achieve a target impedance behaviour on the loudspeaker membrane can be expressed as:

$$i(s) = H_{loc}(s)p(s) + H_{nonloc}(s) \frac{\partial p(s, \mathbf{x})}{\partial \mathbf{x}}, \quad (11)$$

where

$$H_{nonloc}(s) = \frac{Z_m(s)c_a}{Bl Z_{at}(s)s} \times HP, \quad (12)$$

with HP which is a high-pass filter needed in order to avoid the electrical current to go to infinity at low frequencies.

4. Test bench facilities

4.1. Microphones calibration and Thiele-Small cell parameters identification

The microphone calibration and the identification of the Thiele-Small parameters (M, R, C) used in Eq. 3 of each cell have been performed in free field by fitting the impedance curves (normal pressure and normal velocity of the loudspeaker membrane, respectively, measured by a microphone and a laser velocimeter), as explained below.

In open circuit (OC), the current ($i(s)$) is equal to zero and the Eq. 3 writes $Z_m(s)v_n(s) = S_d p(s)$. The impedance in open circuit (Z_{oc}) is:

$$Z_{oc}(s) = \frac{p(s)}{v_n(s)} = \frac{Z_m(s)}{S_d} = \frac{sM}{S_d} + \frac{R}{S_d} + \frac{1}{sCS_d}, \quad (13)$$

the mass (M), compliance (C) and resistance (R) of the loudspeaker over S_d can be identified by fitting the measured impedance curve in open circuit.

In order to identify the force conversion factor (Bl , magnetic field \times winding length), a proportional control is used. In this case, the current ($i(s)$) is $gp(s)$ where g is the gain of the proportional control. Eq. 3 can be written as $Z_m(s)v_n(s) = S_d p(s) - Blgp(s)$, and the impedance with proportional control (Z_{PC}) is:

$$Z_{PC}(s) = \frac{p(s)}{v_n(s)} = \frac{\frac{Z_m(s)}{S_d}}{1 - \frac{Bl}{S_d}g} \quad (14)$$

The force conversion factor over S_d can be identified by fitting the measured impedance curve with proportional control.

The excitation is provided by an external loudspeaker generating a sweep sinus between 50 and 4000Hz, the equivalent acoustic level is 110dB. The Table 1 summarizes the experimental equipment (Fig. 3).

The results of the microphones calibration are provided in Table 2. Sensitivities are expressed after analogical/digital conversion in [Pa/nothing]. The analogical/digital sensitivity is equal to $\frac{2^{12}}{3}$ [nothing/V]. The values of the Thiele-Small parameters of each cells are summarised in Table 3. The averages and the standard deviations are provided in Table 4 for the 5 cells used in this work.

4.2. Caïman wind tunnel test rig

The Caïman wind tunnel is an experimental test bench composed by a straight duct with a square $66 \times 66\text{mm}^2$ section. The

Table 1
Experimental equipment of the microphones calibration and Thiele-Small cell parameters identification.

nb	Description
1	Computer
2	DAC associated to the electronic cells
3	NI 9239 BNC card + cDAQ 9171 (IN)
4	NI 9263 card + cDAQ 9171 (OUT)
5	Audio amplifier
6	Nexus B&K 2692-C (Charge microphones amplifier)
7	Laboratory power supply ($\pm 5V, 2A$ max)
8	Laser velocimeter
9	1/4" microphone B&K 4939 and amplifier B&K 2670
10	Cells and frame
11	Loudspeaker

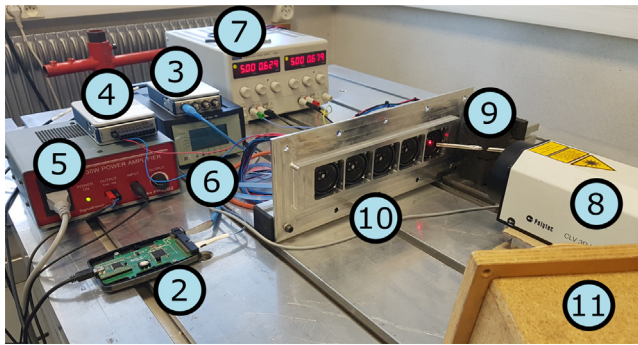


Fig. 3. Experimental setup picture of the microphones calibration and Thiele-Small cell parameters identification.

Table 2
Microphones sensitivities after ADC [Pa/nothing].

Cell	mic A	mic B	mic C	mic D
1: B1	0.1049	0.1109	0.1153	0.0813
2: B2	0.1112	0.1147	0.1061	0.1799
3: B5	0.1252	0.1095	0.0980	0.1032
4: B8	0.1321	0.1144	0.1137	0.1158
5: B10	0.1106	0.0970	0.0847	0.1418

Table 3
Thiele Small parameters.

Cell	M [kg]	R [N.s/m]	C [m/N]	$B\ell$ [T.m]	f_0 [Hz]
1: B1	8.19e-04	0.4938	6.49e-05	1.66	649.1
2: B2	9.13e-04	0.5536	6.77e-05	1.57	653.9
3: B5	8.92e-04	0.7225	6.67e-05	1.68	648.0
4: B8	8.88e-04	0.5611	4.45e-05	1.73	654.1
5: B10	1.26e-03	0.8746	6.34e-05	2.03	672.1

cutoff frequency (f_c) of the tube is 2600Hz. The guided termination reproduces an anechoic condition. Some liners of longitudinal length below 320mm can be tested with a maximum speed flow of Mach 0.4 (137m/s). Acoustic quantities are estimated with a four microphones technique in the plane wave regime. Table 6 summarizes the geometrical parameters. The spacing between

Table 4
Average and standard deviation of Thiele Small parameters and Microphones sensitivities after ADC.

	M [kg]	R [N.s/m]	C [m/N]	$B\ell$ [T.m]	f_0 [Hz]	mic [Pa/nothing]
Average	9.54e-04	0.641	6.34e-05	1.73	655.4	0.114
Standard deviation	1.8e-04	1.6e-01	1.1e-05	1.8e-01	9.7	2.1e-02

pairs of microphones (Δ_{mic}) depends on the frequency range. The Table 5 summarizes the experimental equipment (Figs. 4,5).

Fig. 6a shows the inside view (without wiremesh) of the cells installed in the Caïman wind tunnel. Fig. 6b shows the outside view with the electronic cards, the wires for the electrical supply and the wires for the communication between computer and cells. A rigid panel is installed on the opposite side of the active liner and a wiremesh is glued in front of the cells to protect them from the flow.

4.3. Excitation signals

Experimental tests without flow have been done with a white noise signal between 100Hz and 6000Hz sampled at 51200Hz, with an equivalent acoustic level in the duct of 124dB. The acquisition time is 30 s (30 averages of a period of one second). With flow, the signal to noise ratio was too low to ensure correct measurements with pressure white noise or sweep sinus. Therefore, a pure sinus has been used to increase this ratio and decorrelate the turbulent boundary layer effect from acoustics. The sampling frequency is the same, and the acquisition time is 6 s per frequency (5 averages of a period of one second, the first block being deleted to avoid transient signals).

4.4. Acoustic quantities

Acoustic quantities, used for the post-processing, are defined according to the B&K technical review [33]. The four microphones method is used in order to estimate the transmission (T_a) and reflection (R_a) coefficients for the case of an anechoic termination:

$$T_a = \frac{2e^{ikd}}{T_{11} + \frac{T_{12}}{\rho_0 c_0} + \rho_0 c_0 T_{21} + T_{22}}, \quad (15)$$

where ρ_0, c_0, k and d are respectively the air density, the sound speed, the wave number, the length of the acoustic treatment. T_{ii} are the coefficients of the transfer matrix between the pressure and the velocity at $x = 0$ and $x = d$. The reflection coefficient writes

$$R_a = \frac{T_{11} + \frac{T_{12}}{\rho_0 c_0} - \rho_0 c_0 T_{21} - T_{22}}{T_{11} + \frac{T_{12}}{\rho_0 c_0} + \rho_0 c_0 T_{21} + T_{22}}. \quad (16)$$

Table 5
Experimental equipment of the Caïman wind tunnel tests.

nb	Description
1	Computer
2	DAC associated to the electronic cells
3	NI Pxi card (IN/OUT)
4	Audio amplifier
5	Nexus B&K 2692-C (Charge microphones amplifier)
6	Laboratory power supply ($\pm 5V, 2A$ max)
7	Cells and frame
8	1/4" microphones B&K 4939 and amplifiers B&K 2670
9	Loudspeaker
10	Caïman wind tunnel (straight and square section $66 \times 66mm^2$)
11	Anechoic termination
12	Flow up to Mach 0.4 (137m/s)

Table 6
Geometrical parameters.

x_1	x_2	x_3	x_4	d	Δ_{mic}
$x_2 - \Delta_{mic}$	-0.377 m	$x_4 - \Delta_{mic}$	0.846 m	0.266 m	2.2 cm or 10 cm

The transmission loss (TL) is defined using the transmission coefficient:

$$TL = 10 \log_{10} \left(\frac{1}{|T_a|^2} \right), \tag{17}$$

and the absorption coefficient (α) using both transmission and reflection coefficients:

$$\alpha = 1 - |T_a|^2 - |R_a|^2. \tag{18}$$

In order to compare different treatments by experimental measurements, the insertion loss is used as an indicator, computed from the transmission loss difference between a treated duct and the rigid one:

$$IL = TL - TL_{rigid}. \tag{19}$$

Acoustic equivalent levels are estimated in dB with $P_{ref} = 20 \mu Pa$ the reference pressure:

$$L_{eq} = 20 \log_{10} \left(\frac{P}{P_{ref}} \right). \tag{20}$$

5. Experimental results

5.1. Characterization of local control without flow

This subsection presents the results with a local control law without flow.

For these first results, a set of four curves are presented:

- the reflection coefficient ($|R_a|$),
- the transmission coefficient ($|T_a|$),

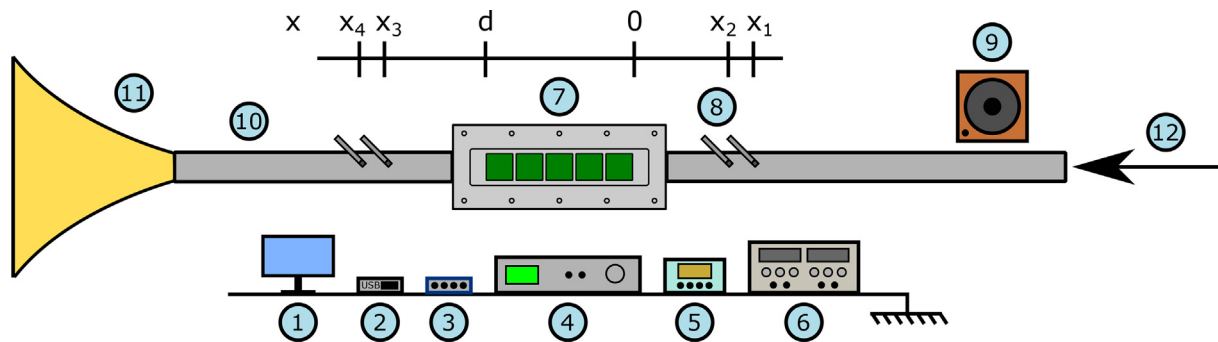


Fig. 4. Experimental setup diagram of the Caïman wind tunnel tests.

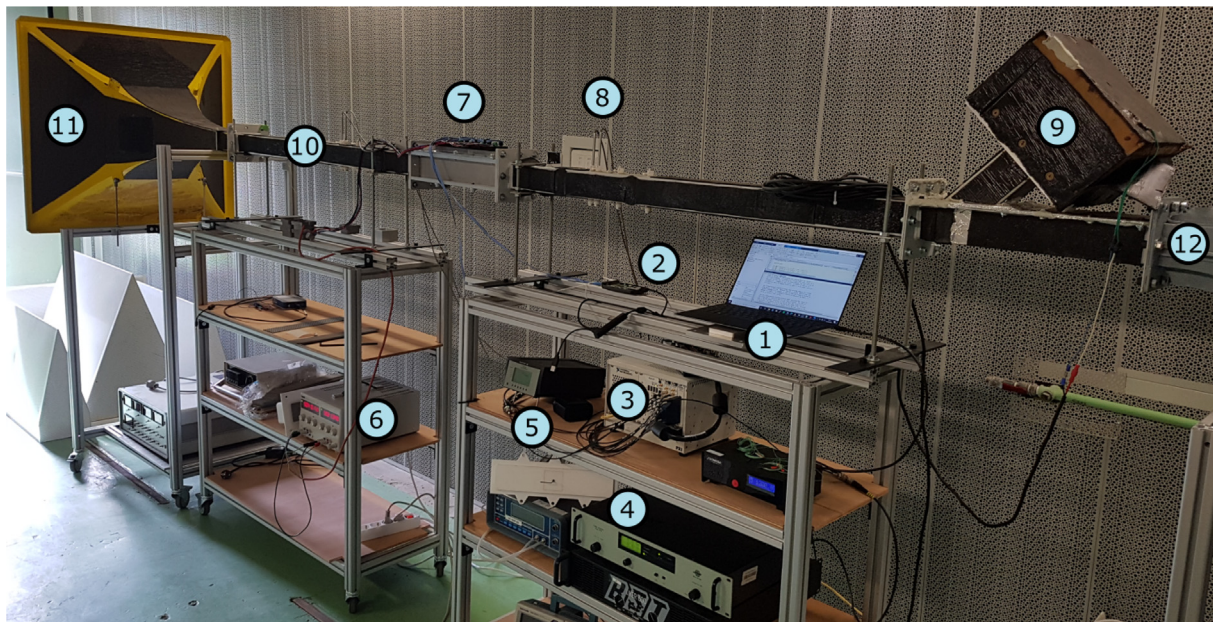


Fig. 5. Experimental setup picture of the Caïman wind tunnel tests.

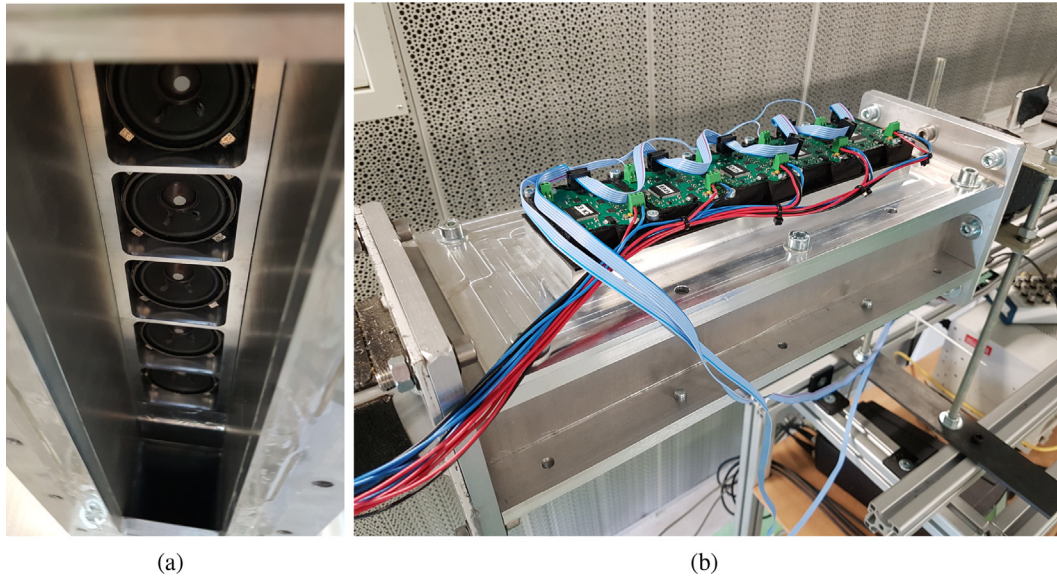


Fig. 6. Active cells mounted in the Caïman wind tunnel: a) inside view (without wiremesh), b) outside view.

- the absorption coefficient (α),
- the insertion loss (IL).

The frequency bandwidth where the control is efficient is named efficiency zone which is located around the resonance frequency of the locally controlled loudspeaker. Center frequency of the each efficiency zone is defined as:

$$f_{eff} = f_0 \sqrt{\frac{\mu_2}{\mu_1}} \quad (21)$$

These frequencies depending on the parameters μ_1 and μ_2 are given in Table 7. When these two parameters are equal, the control is efficient around the natural frequency of the loudspeaker (f_0). The minimum value of the μ_1 parameter of the local control law ensuring

Table 7
Efficient frequencies (f_{eff}) depending on the parameters μ_1 and μ_2 .

μ_1	μ_2	f_{eff}
0.4	0.4	$mean(f_0) = 655\text{Hz}$
0.4	1	1036Hz
0.4	2	1465Hz
0.4	0.2	463Hz
0.4	0.1	327Hz

the stability of the system is equal to 0.4. The μ_1 parameter is constant as it is fixed by high frequency stability constraints, therefore the μ_2 parameter is used to tune the frequency f_{eff} where the control is efficient.

[Figs. 7, 8] show the performances of the control when the target resistance varies to $\rho_0 c_0$, $2\rho_0 c_0$ and $0.5\rho_0 c_0$. The μ_1 and μ_2 parameters of the local control law are equal to 0.4.

The reflection coefficient ($|R_a|$) and the transmission coefficient ($|T_a|$) are presented only for these first results. For the following results in this document, the authors have chosen to present only the absorption coefficient and the insertion loss using the formulas presented in the Section 4.4.

Performance in terms of acoustic absorption increases around the f_{eff} frequency when the target resistance decreases (Figs. 8). The insertion loss without control is equal to 6.5dB. For the target resistance ($2\rho_0 c_0$), the acoustic quantity (IL) is slightly lower equal to 5.3dB. The value goes from 7.2dB to 9.8dB when the target resistance decreases from $\rho_0 c_0$ to $0.5\rho_0 c_0$.

Figs. 9 shows the performances of the control when the parameters of the control law are varied. The μ_1 parameter of the local law is 0.4 and μ_2 is changed and takes values: 0.2, 0.4, 1, 2. The target resistance is equal to $0.5\rho_0 c_0$. In order to reduce the noise at low frequencies ($\mu_2 = 0.2$), the spacing between pairs of microphones (Δ_{mic}) has been increased from 2.2cm to 10cm.

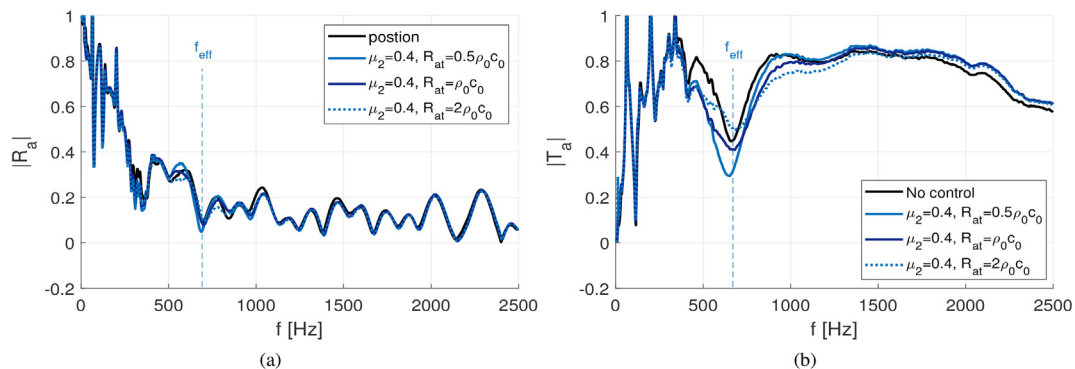


Fig. 7. Effect of the variation of the target resistance ($R_{at} = [0.5\rho_0 c_0, \rho_0 c_0, 2\rho_0 c_0]$) and control law parameters ($\mu_1 = \mu_2 = 0.4$): a) Reflexion coefficient ($|R_a|$), b) Transmission coefficient ($|T_a|$).

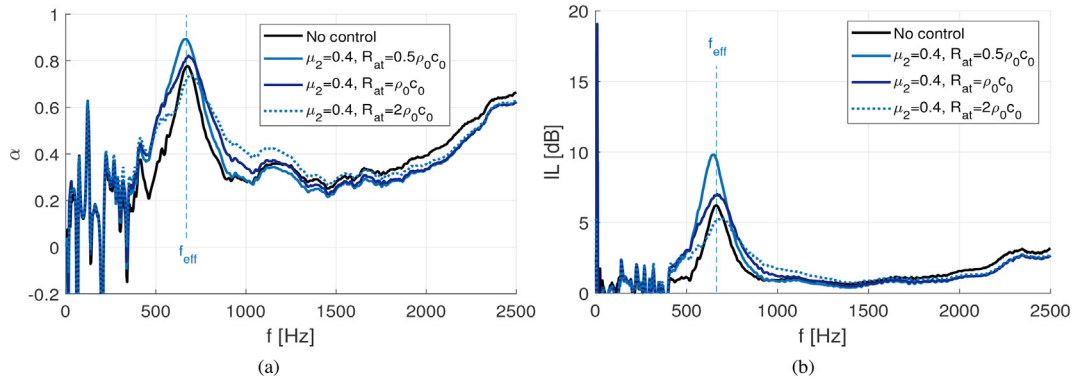


Fig. 8. Effect of the variation of the target resistance ($R_{at} = [0.5\rho_0c_0, \rho_0c_0, 2\rho_0c_0]$) and control law parameters ($\mu_1 = \mu_2 = 0.4$): a) Absorption coefficient (α), b) Insertion loss (IL).

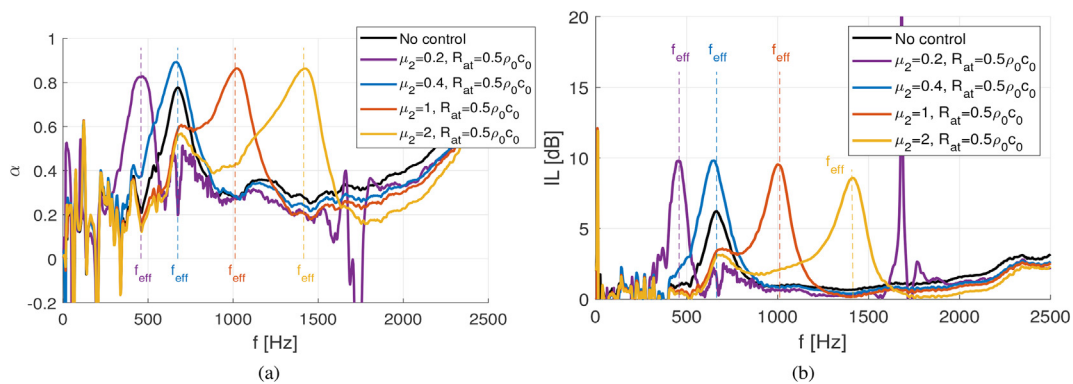


Fig. 9. Effect of the variation of the parameters of the control law ($\mu_1 = 0.4, \mu_2 = [0.2, 0.4, 1, 2]$) and target resistance ($R_{at} = 0.5\rho_0c_0$): a) Absorption coefficient (α), b) Insertion loss (IL).

Consequently, a zero pressure measurement is present at 1700Hz corresponding to a half wavelength ($\lambda/2$) equal to 10cm (the spacing between pairs of microphones).

5.2. Characterization of non-local control without flow

This subsection presents the experimental results with a non-local control law and no flow.

Figs. 10 compare the results relative to the two different control strategies (local and non-local control). The target resistance (R_{at}) is equal to $0.5\rho_0c_0$. μ_1 is chosen equal to 0.4 for both local and non-local strategies while the parameter μ_2 takes values: 0.2, 0.4, 1, 2. The advection velocity c_a (H_{nonloc}) is equal to $0.9c_0$ and the cut-on frequency of the HP filter in Eq. 12 is put at 50Hz. An additional absorption and a mean increase of insertion loss of about 3.5dB is observed either at f_{eff} when the non-local control is applied.

Figs. 11 present the absorption and insertion loss evolution when the target resistance is varying between $\rho_0c_0, 2\rho_0c_0$ and $0.5\rho_0c_0$. The μ_1 and μ_2 parameters of the local and non-local control laws are equal to 0.4. The advection velocity c_a stays at $0.9c_0$ and the first order highpass filter at 50Hz is used. It can be confirmed here that the performances are increased around the f_{eff} frequency when the target resistance decreases. The insertion loss, without control, at $f_{eff} = f_0$ is equal to 6.5dB. For target resistance equal to $2\rho_0c_0$, the IL is 5.9dB. The values IL goes from 8.8dB to 12.1dB when the target resistance decreases from ρ_0c_0 to $0.5\rho_0c_0$. The results confirm the adaptability and the stability of the whole system with the non-local control strategy.

5.3. Tests without flow - Summary tables

In order to highlight the major trends in the acoustic properties of the active acoustic liner, different indicators are computed on the frequency band of interest from 200 to 1500Hz:

- maximum insertion loss (IL_{max}) and average insertion loss (IL_{mean}): Table 8,
- maximum absorption coefficient (α_{max}) and average absorption coefficient (α_{mean}): Table 9.

The objective in this part is to observe the change of absorption and insertion loss when the targeted impedance (R_{at}) is varying. The best result for the considered indicator is highlighted in orange for the local control and in red for the non-local control. The reference value for the non-controlled configuration is given in the first line of the table. The maximum insertion loss (IL_{max}) has similar values when the μ_2 parameters is varying for a chosen controller or target resistance. The table is used to compare the performance of the control between the local and the non-local control for different values of target resistance.

Table 10 summarizes the variation of performances achieved by the non-local control strategy with respect to the local one. Indicators are averaged for all μ_2 parameters and the difference between the non-local and the local strategies is calculated for each target resistance. The increase in efficiency in terms of maximum of insertion loss (IL_{max}) is higher for high targeted impedance values. Regarding the maximum absorption coefficient indicator (α_{max}), the contribution of non-local control is less important for low values of target resistance.

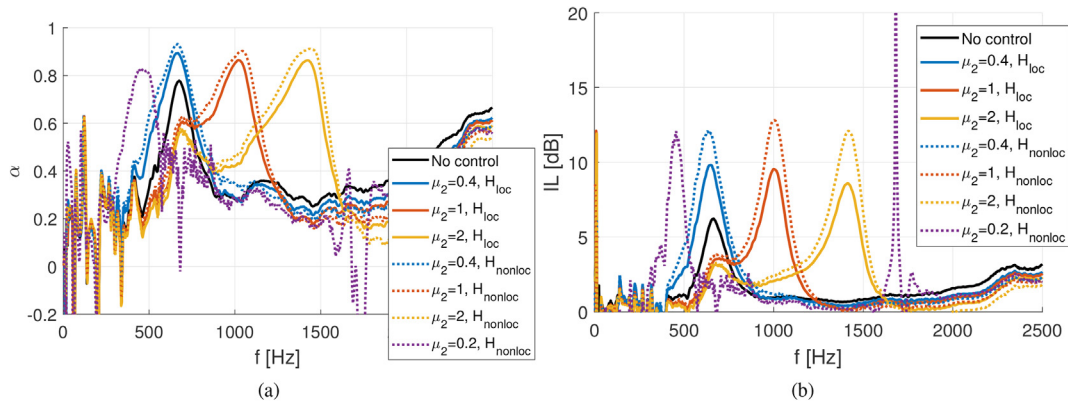


Fig. 10. Effect of the variation of the parameters of the control law ($\mu_1 = 0.4, \mu_2 = [0.2, 0.4, 1, 2]$) and target resistance ($R_{at} = 0.5\rho_0c_0$). Transport speed of the advection condition ($H_{nonloc} : c_a = 0.9c_0$): a) Absorption coefficient (α), b) Insertion loss (IL).

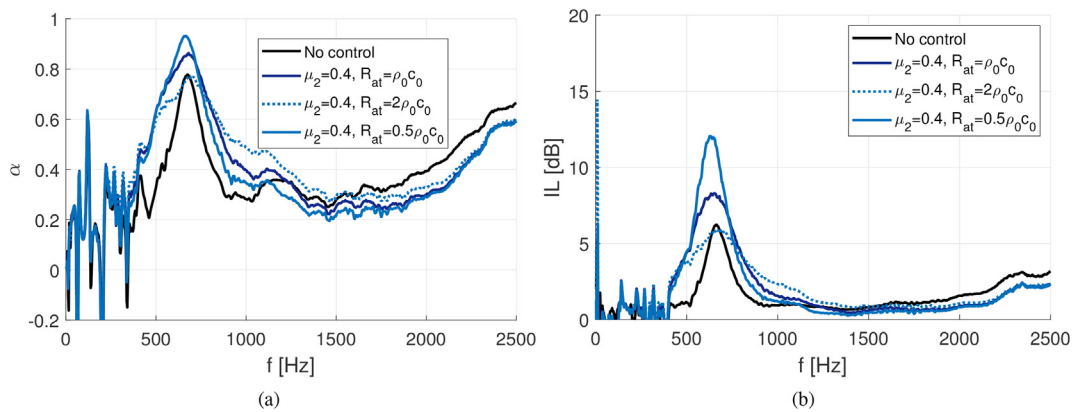


Fig. 11. Effect of the variation of the target resistance ($R_{at} = [\rho_0c_0, 2\rho_0c_0, 0.5\rho_0c_0]$) and control law parameters ($\mu_1 = \mu_2 = 0.4$). Transport speed of the advection condition ($H_{nonloc} : c_a = 0.9c_0$): a) Absorption coefficient (α), b) Insertion loss (IL).

Table 8

Values of Maximum Insertion loss (IL_{max}) [dB] and Average Insertion loss (IL_{mean}) [dB] for local and non-local controls ($\mu_1 = 0.4, c_a = 0.9c_0$).

IL_{max} (IL_{mean}) [dB]	Control	μ_2	0.2	0.4	1	2
R_{at}						
∞	No control		6.5 (1.7)			
$0.5\rho_0c_0$	H_{loc}		9.8 (1.5)	9.8 (2.1)	9.5 (2.2)	8.6 (2.5)
	H_{nonloc}		12.1 (1.8)	12.1 (2.6)	12.8 (2.9)	12.1 (3.1)
ρ_0c_0	H_{loc}		5.9 (1.5)	7.2 (2.3)	6.7 (2.4)	6.2 (2.5)
	H_{nonloc}		7.4 (1.8)	8.8 (2.8)	9.1 (3.0)	8.5 (3.0)
$2\rho_0c_0$	H_{loc}		3.6 (1.4)	5.3 (2.0)	4.3 (2.1)	4.0 (2.0)
	H_{nonloc}		4.3 (1.8)	5.9 (2.5)	5.7 (2.6)	5.4 (2.4)

Table 9

Values of Maximum Absorption coefficient (α_{max}) and Average Absorption coefficient (α_{mean}) for local and non-local controls ($\mu_1 = 0.4, c_a = 0.9c_0$).

α_{max} (α_{mean}) [dB]	Control	μ_2	0.2	0.4	1	2
R_{at}						
∞	No control		0.80 (0.39)			
$0.5\rho_0c_0$	H_{loc}		0.83 (0.36)	0.89 (0.39)	0.86 (0.41)	0.86 (0.45)
	H_{nonloc}		0.93 (0.37)	0.93 (0.42)	0.90 (0.44)	0.91 (0.48)
ρ_0c_0	H_{loc}		0.75 (0.39)	0.84 (0.44)	0.78 (0.46)	0.79 (0.48)
	H_{nonloc}		0.80 (0.41)	0.88 (0.48)	0.85 (0.49)	0.86 (0.50)
$2\rho_0c_0$	H_{loc}		0.63 (0.41)	0.74 (0.43)	0.65 (0.44)	0.66 (0.43)
	H_{nonloc}		0.67 (0.44)	0.77 (0.48)	0.74 (0.48)	0.75 (0.47)

Table 10
Increase in efficiency due to non-local control.

	R_{at}	IL_{max}	IL_{mean}	α_{max}	α_{mean}
$H_{nonloc} - H_{loc}$ [dB]	$0.5\rho_0c_0$	2.8	0.4	0.03	0.03
	ρ_0c_0	1.9	0.4	0.06	0.03
	$2\rho_0c_0$	1.1	0.4	0.06	0.04

Table 11 summarizes the evolutions of the indicators when the targeted impedance moves from $2\rho_0c_0$ to ρ_0c_0 and from ρ_0c_0 to $0.5\rho_0c_0$. Indicators are averaged for all μ_2 parameters and the two control strategies, the difference is first calculated between the target resistance ρ_0c_0 and $2\rho_0c_0$ and then between ρ_0c_0 and $0.5\rho_0c_0$. The performances increases when the target resistance decreases, the indicators of Table 11 highlight the gain obtained between the different target resistance values which decrease. When the target resistance is divided by two, the maximum insertion loss (IL_{max}) is increased by about 3dB and the maximum absorption coefficient (α_{max}) by approximately 0.1. Overall, the average of the indicators (IL_{mean} and α_{mean}) decreases for the change of the target resistance from ρ_0c_0 to $0.5\rho_0c_0$.

5.4. Characterization of local control at different flow speeds

This subsection presents the acoustical performances with an applied local control law under a fluid flow. The targeted impedance has been selected as $R_{at} = 0.5\rho_0c_0$.

The flow speeds (in the center of the flow in the duct) are: 20, 40, 60, 80, 100 and 120m/s (*Mach*0.06, 0.12, 0.18, 0.24, 0.29 and 0.35). Figs. 12 present acoustic absorption and insertion loss when the flow speeds increase. The μ_1 and μ_2 parameters of the local control law are equal to 0.4. The reference test without flow is plotted with a deep blue solid line. As a reminder, with flow, a pure sinus has been used to increase the signal to noise ratio, each curve marker correspond to the result induced by a tonal excitation

Figs. 13 present the same results when μ_2 control parameter varies between 0.4, 1, 2. The flow speed is equal to 100m/s (*Mach*0.29).

Table 11
Changing target resistance average effect on the indicators for the two control strategies.

R_{at}	IL_{max}	IL_{mean}	α_{max}	α_{mean}
$2\rho_0c_0 \rightarrow \rho_0c_0$ [dB]	2.7	0.3	0.12	0.01
$\rho_0c_0 \rightarrow 0.5\rho_0c_0$ [dB]	3.4	-0.1	0.06	-0.04

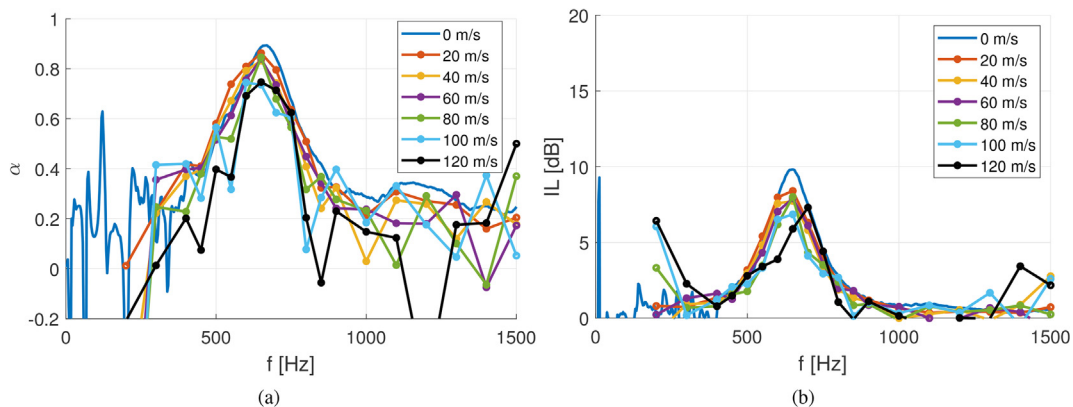


Fig. 12. Effect of the variation of flow velocity [20, 40, 60, 80, 100, 120]m/s and control law parameters ($\mu_1 = \mu_2 = 0.4$): a) Absorption coefficient (α), b) Insertion loss (IL).

These results validate the adaptability and the stability of the system between 300 and 1500Hz with the tested parameters of local control law with different flow velocities.

5.5. Characterization of non-local control at different flow speeds

This subsection presents the results with a non-local control law and external fluid flow.

The flow speed is equal to 20, 40, 60, 80 and 100m/s (*Mach*0.06, 0.12, 0.18, 0.24 and 0.29). The advection velocity c_a (H_{nonloc}) is equal to $0.9c_0$ and the first-order highpass filter at 50Hz has been added.

Figs. 14 present the acoustical performances when the flow speed increase. The μ_1 and μ_2 parameters of the local and non-local control laws are equal to 0.4.

The non-local control also works with fluid flow with better performances than the local one.

5.6. Tests with flow - Summary tables

One present here the overall performances obtained with fluid flow. The indicators are the same as before:

- maximum insertion loss (IL_{max}) and average insertion loss (IL_{mean}): Table 12,
- maximum absorption coefficient (α_{max}) and average absorption coefficient (α_{mean}): Table 13.

In the part, a focus is done on the evolution of absorption and insertion loss when the flow speed is varying. As before, the same convention is used, the best result for the considered indicator is highlighted in orange for the local control and in red for the non-local control. The maximum insertion loss (IL_{max}) is always greater for the non-local control than the local control strategy in the majority of cases. Exceptions can be highlight at high speed (80 et 100 m/s) for weak μ_2 (0.2 and 0.4), that can be due to low signal to noise ratio. It would probably be necessary to adjust the advection speed for high flow speeds. This is normal, the flow is not supposed to change the conclusions done without flow regarding the difference between the local and non-local control. The air flow slightly reduces the performance around the f_{eff} while keeping the effect of control and adaptability.

6. Effective Impedance

The impedance eduction process consists in minimizing the difference between the measured and computed TL and α indicators

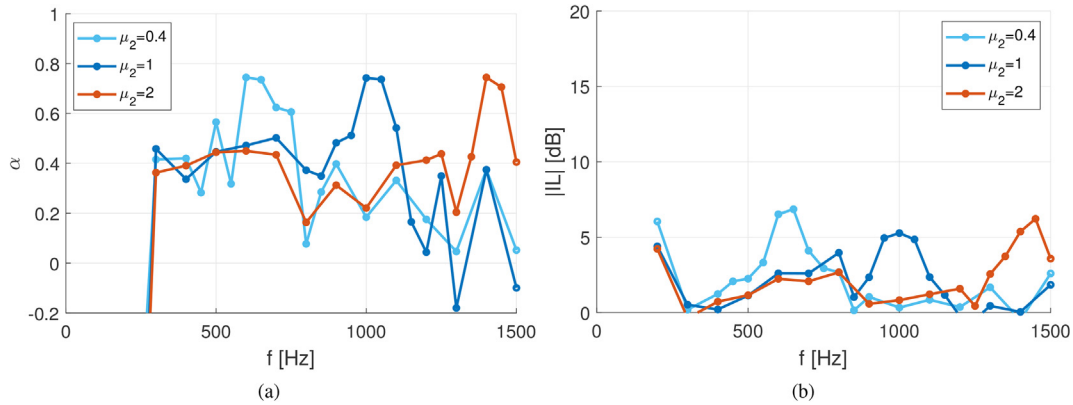


Fig. 13. Effect of the variation of the parameters of the control law ($\mu_1 = 0.4, \mu_2 = [0.4, 1, 2]$) and flow velocity (100m/s): a) Absorption coefficient (α), b) Insertion loss (IL).

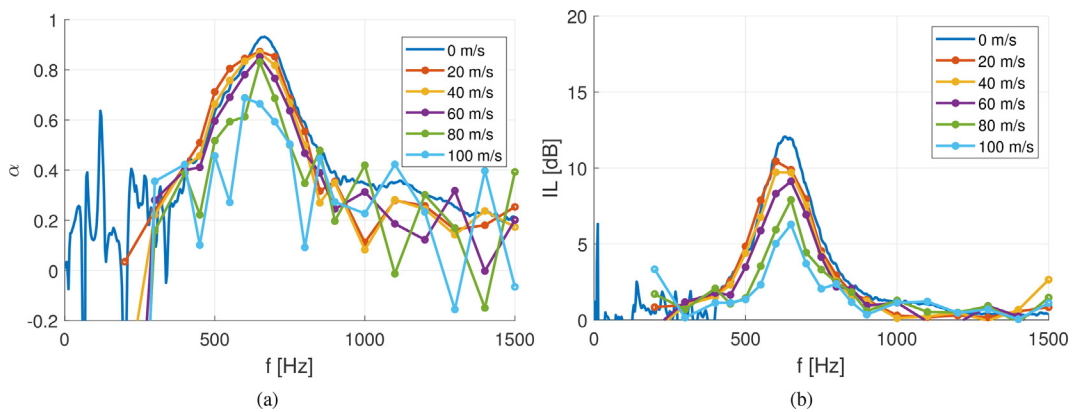


Fig. 14. Effect of the variation of flow velocity [20, 40, 60, 80, 100]m/s and control law parameters ($\mu_1 = \mu_2 = 0.4$). Transport speed of the advection condition ($H_{nonloc} : c_a = 0.9c_0$): a) Absorption coefficient (α), b) Insertion loss (IL).

Table 12

Values of Maximum Insertion loss (IL_{max}) [dB] and Average Insertion loss (IL_{mean}) [dB] with flow for local and non-local controls ($\mu_1 = 0.4, c_a = 0.9c_0, R_{at} = 0.5\rho_0c_0$).

Control	flow	μ_2			
		0.2	0.4	1	2
H_{loc}	20 m/s	5.4 (1.6)	8.4 (2.5)	8.2 (2.4)	8.0 (2.8)
	40 m/s	5.9 (1.5)	7.7 (2.3)	7.0 (2.3)	7.4 (2.7)
	60 m/s	4.8 (1.3)	7.9 (2.2)	7.7 (2.0)	8.1 (2.4)
	80 m/s	4.7 (1.8)	8.0 (2.1)	6.2 (2.1)	6.9 (2.4)
	100 m/s	4.3 (1.9)	6.9 (2.4)	5.3 (2.1)	6.2 (2.3)
	120 m/s		7.3 (2.4)		
H_{nonloc}	20 m/s	7.0 (1.7)	10.4 (3.2)	10.2 (3.1)	10.9 (3.5)
	40 m/s	6.9 (1.6)	9.7 (2.9)	9.7 (2.8)	10.1 (3.3)
	60 m/s	4.9 (1.5)	9.1 (2.5)	9.7 (2.5)	10.2 (3.0)
	80 m/s	3.9 (1.7)	7.9 (2.2)	7.7 (2.5)	8.9 (3.1)
	100 m/s		6.3 (1.8)	5.7 (2.0)	7.8 (2.4)

by adjusting the equivalent implemented numerical impedance. In the 3D numerical model, using a finite element software (Comsol), acoustic module is used and the problem is modeled in the frequency domain via the Helmholtz equation. The impedance is applied on the liner surface as a complex number $Z(\omega) = a(\omega) + ib(\omega)$. As one wants to respect the dynamical form of our synthesized impedance with a negative imaginary part ($Im(Z)$) before the f_{eff} frequency and positive one after. One chooses to search an impedance satisfying this condition:

$$Z_{fitted}(s) = M_{eff}s + R_{eff} + K_{eff}/s. \tag{22}$$

The values of the effective parameters (M_{eff}, R_{eff} and K_{eff}) are found by minimising the cost function $f = |T_{a_{num}} - T_{a_{exp}}| + |R_{a_{num}} - R_{a_{exp}}|$, where $T_{a_{num}}$ and $R_{a_{num}}$ are respectively the transmission and the reflection coefficients obtained with the numerical model, $T_{a_{exp}}$ and $R_{a_{exp}}$ are the corresponding experimental quantities.

Fig. 15 presents the geometry used in the numerical model. The dimensions of the geometry are same as the Caïman wind tunnel

Table 13
 Values of Maximum Absorption coefficient (α_{max}) and Average Absorption coefficient (α_{mean}) with flow for local and non-local controls ($\mu_1 = 0.4, c_a = 0.9c_0, R_{at} = 0.5\rho_0c_0$).

α_{max} (α_{mean}) Control	μ_2	0.2	0.4	1	2
	flow				
H_{loc}	20 m/s	0.74 (0.32)	0.86 (0.42)	0.82 (0.42)	0.81 (0.45)
	40 m/s	0.74 (0.22)	0.83 (0.35)	0.82 (0.37)	0.80 (0.39)
	60 m/s	0.68 (0.09)	0.84 (0.32)	0.82 (0.28)	0.76 (0.30)
	80 m/s	0.56 (0.07)	0.85 (0.28)	0.80 (0.22)	0.69 (0.25)
	100 m/s	0.55 (-0.07)	0.74 (0.26)	0.74 (0.21)	0.74 (0.23)
	120 m/s		0.75 (0.24)		
H_{nonloc}	20 m/s	0.76 (0.32)	0.87 (0.44)	0.88 (0.46)	0.89 (0.49)
	40 m/s	0.74 (0.22)	0.87 (0.39)	0.88 (0.40)	0.87 (0.42)
	60 m/s	0.66 (0.11)	0.85 (0.32)	0.88 (0.31)	0.81 (0.32)
	80 m/s	0.64 (-0.01)	0.83 (0.23)	0.85 (0.25)	0.77 (0.29)
	100 m/s		0.69 (0.13)	0.74 (0.10)	0.72 (0.14)

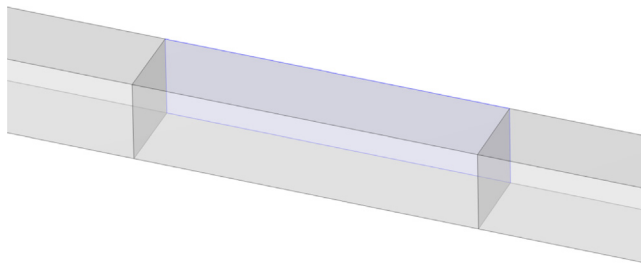


Fig. 15. Numerical model for the impedance reduction equivalent in terms of geometry of the Caiman wind tunnel test rig..

test bench. The anechoic termination is defined by a Sommerfeld condition at the end of the duct to avoid wave reflections. A plane wave in the frequency domain is generated at the beginning of the duct.

6.1. Local control

Figs. 16 shows the experimental absorption coefficient and the insertion loss (curves with lines) presented in Section 5.1, with $R_{at} = 0.5\rho_0c_0$. The μ_1 parameter of the local control law is equal to 0.4 and the μ_2 parameter takes the value 0.2, 0.4, 1, 2, 0.2. The curves with circle markers correspond to the numerical results of the impedance reduction associated to each experimental curves.

The fitting works well on the configurations without control and with control ($\mu_1 = \mu_2, f_{eff} = f_0$) because the model is in ade-

quacy with physics. The computed impedance is based on a one degree of freedom model (Eq. 22). For the configuration when $\mu_1 \neq \mu_2$, performances are well estimates around f_{eff} . Due to the time delay in the controller and the variation of the dynamic parameters of the loudspeaker model according to its acoustic environment, energy is absorbed around the natural frequency of the loudspeaker (f_0) even if the control is tuned with an efficiency frequency (f_{eff}) different from the natural frequency of the loudspeaker (f_0). This is not disturbing as it increases the efficiency of the broadband control without affecting the stability. The model can be improved with a two degrees of freedom model for the computed impedance. Effective parameters are given in the Section 6.3.

6.2. Non-local control

Figs. 17 present the experimental absorption coefficient and the insertion loss (curves with lines) presented in Section 5.2 with $R_{at} = 0.5\rho_0c_0$, which concern non non-local control. The authors are aware of using a local impedance model to characterize non-local behaviour. Aeronautical engineers use this impedance model to compare the different treatments.

6.3. Impedance

The fitted impedance parameters using numerical results are summarized in **Table 14**. The **Fig. 18** shows the effective impedance on the liner surface computed from the numerical model.

The parameters of the Eq. 6, Thiele Small parameters of the loudspeaker (M and K) and target resistance (R_{at}), can be retrieved

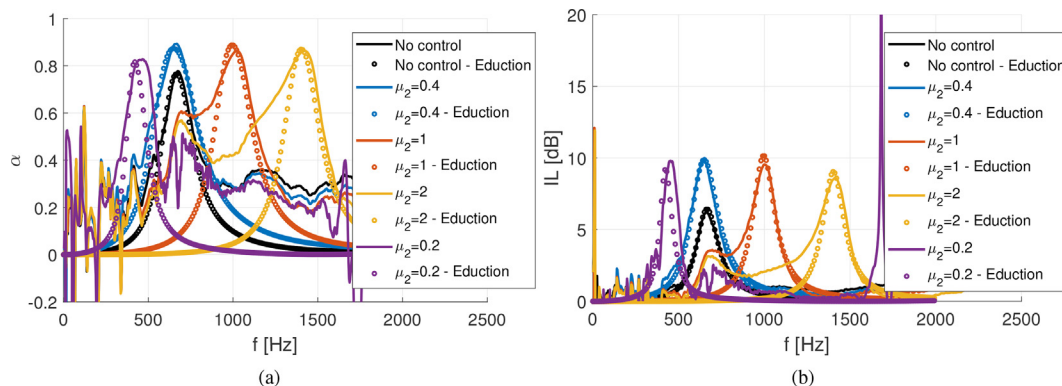


Fig. 16. Education - Variation of the parameters of the control law ($\mu_1 = 0.4, \mu_2 = [0.2, 0.4, 1, 2]$), Target resistance ($R_{at} = 0.5\rho_0c_0$): a) Absorption coefficient (α), b) Insertion loss (IL).

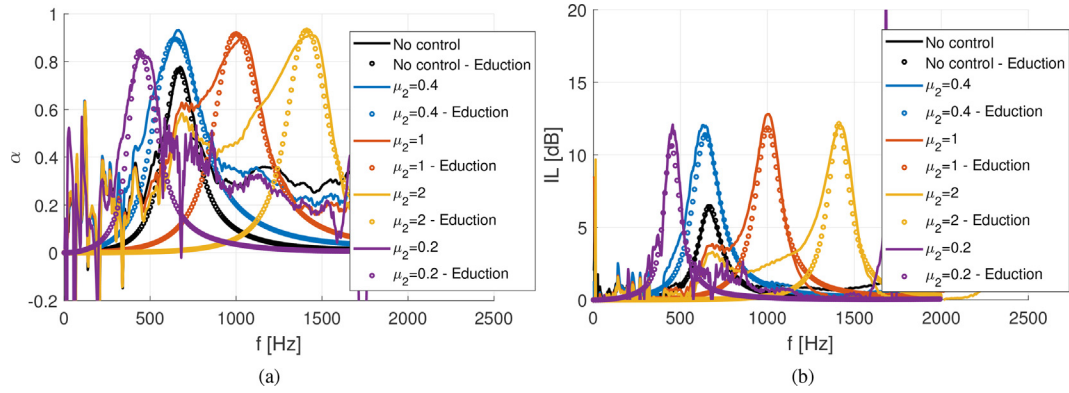


Fig. 17. Education - Variation of the parameters of the control law ($\mu_1 = 0.4, \mu_2 = [0.2, 0.4, 1, 2]$), Transport speed of the advection condition ($H_{nonloc} : c_a = 0.9c_0$), Target resistance ($R_{at} = 0.5\rho_0c_0$): a) Absorption coefficient (α), b) Insertion loss (IL).

Table 14
Fitted impedance parameters using experimental results.

Configuration	M_{eff}	R_{eff}	K_{eff}
No control	1.1288	1.1319e + 03	1.9690e + 07
$\mu_2 = 0.4, H_{loc}$	0.6021	720.3010	9.9413e + 06
$\mu_2 = 1, H_{loc}$	0.7133	720.3010	2.8404e + 07
$\mu_2 = 2, H_{loc}$	0.8000	823.2010	6.3582e + 07
$\mu_2 = 0.2, H_{loc}$	1.4585	720.3010	1.0150e + 07
$\mu_2 = 0.4, H_{nonloc}$	0.5325	617.4010	8.6682e + 06
$\mu_2 = 1, H_{nonloc}$	0.5315	617.4010	2.1495e + 07
$\mu_2 = 2, H_{nonloc}$	0.5998	617.4010	4.8543e + 07
$\mu_2 = 0.2, H_{nonloc}$	0.9669	617.4010	7.4075e + 06

Table 15
Comparison between Thiele Small parameters of the loudspeaker (M and K) and target resistance (R_{at}) and reassessed one from effective parameters.

Configuration	$M_{eff} \frac{S_d}{\mu_1 S_{cell}}$	$R_{eff} \frac{S_d}{S_{cell}}$	$\frac{1}{K_{eff} \frac{S_d}{\mu_2 S_{cell}}}$
$\mu_2 = 0.4, H_{loc}$	6.57e-04	236	9.22e-05
$\mu_2 = 1, H_{loc}$	7.78e-04	226	8.07e-05
$\mu_2 = 2, H_{loc}$	8.73e-04	269	7.21e-05
$\mu_2 = 0.2, H_{loc}$	1.60e-03	236	4.52e-05
Average	9.77e-04	244	7.25e-05
Thiele Small parameters & Target resistance	M	$R_{at} = 0.5\rho_0c_0$	C
Average	9.54e-04	205.8	6.34e-05
$\epsilon[\%]$	-2.3%	-15.8%	-12.6%

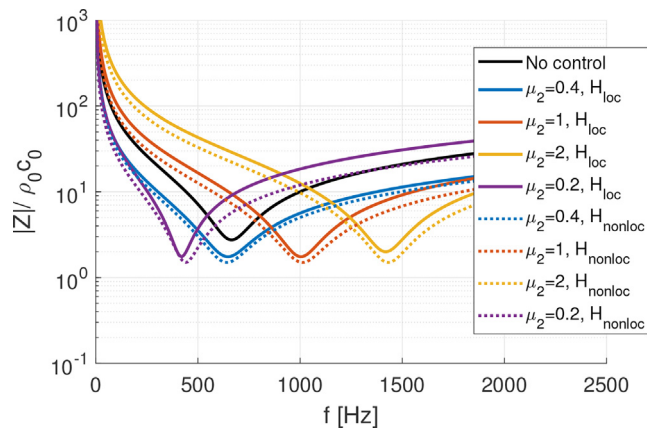


Fig. 18. Effective impedance in the treated surface for experimental results.

using the effective parameters of the different fitted impedances (Eq. 22) multiplied by the ratio S_d/S_{cell} where S_{cell} is the area of the cell. Indeed, the target impedance is experimentally defined only on the surface of the membranes of each loudspeakers and the rest of the active liner area is rigid.

From the effective parameters, Thiele Small parameters of the loudspeaker (M and K) and target resistance (R_{at}) are evaluated and result for the local control are summarized in Table 15. The reassessed mass (resp. compliance) is on average equal to $9.54e^{-04}kg$ ($7.25e^{-05}[m/N]$) with an error of 2.3% (resp. 12.6%) compared to the real mass M (resp. compliance C). The target resistance is overvalued of 15.8% from the effective resistance.

The differences observed can be explained by the complexity of cell and the wiremesh of the liner that is not modelled in the simplified numerical model. The resistance of the wiremesh has been experimental estimated and increase the target resistance of 10%.

The dynamics of the system are well reproduced and the results obtained with the effective impedance are consistent with the experimental results.

7. Conclusion

In this article, an acoustic characterisation of a 2D active liner based on an array of electroacoustic absorbers is presented. The control law is implemented by pressure-based, current-driven digital architecture for impedance control. Both local and non-local control strategies are experimentally validated without and with air flow on the Caïman wind tunnel test rig. Frequencies where the control is efficient depending on the parameters μ_1 and μ_2 of the control law. The minimum value of the μ_1 parameter of the local and non-local control law ensuring the stability of the system is equal to 0.4. The adaptability and the stability of the system between 300 and 1500Hz with the tested parameters of local and the non-local control laws have been validated. Different indicators are computed (maximum and average insertion loss and absorption coefficient on the frequency band of interest) to compare the configurations. The non-local control strategy present better performances than the local one. In both control strategies, when the target resistance is divided by two, the maximum insertion loss is increased by about 3dB and the maximum absorption coefficient by approximately 0.1. With flow, the excitation signal and the acquisition procedure has been adapt to increase the signal to noise ratio. Both local and non-local control also works with fluid

flow until Mach 0.29 and the adaptability and the stability is assured with different flow velocity. The air flow slightly reduces the performance. Finally, an impedance reduction method with a numerical model is used to identify the experimental surface equivalent impedance of the active liner. The computed impedance is based on a one degree of freedom model. This local impedance model is also used to fit the non-local experimental results for engineering reasons. From the effective parameters, Thiele Small parameters of the loudspeaker (M and K) and target resistance (R_{it}) can be retrieved using the effective parameters of the different fitted multiplied by an area ratio between the treated surface (membranes of each loudspeakers) and the total area of the active liner. The dynamics of the system are well reproduced and the results obtained with the effective impedance are consistent with the experimental results.

CRediT authorship contribution statement

K. Billon: Investigation, Formal analysis, Writing - original draft, Writing - review & editing. **E. De Bono:** Methodology. **M. Perez:** Methodology. **E. Salze:** Supervision. **G. Matten:** Conceptualization, Methodology. **M. Gillet:** Methodology. **M. Ouisse:** Supervision. **M. Volery:** Methodology. **H. Lissek:** Supervision. **M. Collet:** Supervision, Project administration, Funding acquisition.

Declaration of Competing Interest

The authors declare that they have no known competing financial interests or personal relationships that could have appeared to influence the work reported in this paper.

Acknowledgements

The SALUTE project has received funding from the Clean Sky 2 Joint Undertaking under the European Union's Horizon 2020 research and innovation programme under grant agreement No 821093. This publication reflects only the author's view and the JU is not responsible for any use that may be made of the information it contains.

References

- [1] Cremer L. Theory regarding the attenuation of sound transmitted by air in a rectangular duct with an absorbing wall, and the maximum attenuation constant produced during this process. *Acta Acust* 1953;3:249.
- [2] Tester B. The optimization of modal sound attenuation in ducts, in the absence of mean flow. *J Sound Vib* 1973;27:477–513.
- [3] Tester B. The propagation and attenuation of sound in lined ducts containing uniform or "plug" flow. *J Sound Vib* 1973;28:151–203.
- [4] Guess A. Calculation of perforated plate liner parameters from specified acoustic resistance and reactance. *J Sound Vib* 1975;40:119–37.
- [5] Jones M, Tracy M, Watson W, Parrott T. Effects of liner geometry on acoustic impedance. In: 8th AIAA/CEAS Aeroacoustics Conference & Exhibit. p. 2446.
- [6] A.S. Hersh, J. Tso, Extended frequency range helmholtz resonators, 1992. US Patent 5,119,427.
- [7] Matsuhisa H, Ren B, Sato S. Semiactive control of duct noise by a volume-variable resonator. *JSME Int J Ser* 1992;3(35):223–8.
- [8] de Bedout JM, Franchek MA, Bernhard RJ, Mongeau L. Adaptive-passive noise control with self-tuning helmholtz resonators. *J Sound Vib* 1997;202:109–23.
- [9] Estève SJ, Johnson ME. Adaptive helmholtz resonators and passive vibration absorbers for cylinder interior noise control. *J Sound Vib* 2005;288:1105–30.
- [10] Abbad A, Rabenorosoa K, Ouisse M, Atalla N. Adaptive helmholtz resonator based on electroactive polymers: modeling, characterization, and control. *Smart Mater Struc* 2018;27:105029.
- [11] Benouhiba A, Rougeot P, Andreff N, Rabenorosoa K, Ouisse M. Origami-based auxetic tunable helmholtz resonator for noise control. *Smart Mater Struc* 2021;30:035029.
- [12] Horowitz S, Nishida T, Cattafesta III L, Sheplak M. Characterization of a compliant-backplate helmholtz resonator for an electromechanical acoustic liner. *Int J Aeroacoustics* 2002;1:183–205.
- [13] Lissek H, Rivet E, Karkar S, Boulandet R. Design of active multiple-degrees-of-freedom electroacoustic resonators for use as broadband sound absorbers (2017).
- [14] Lissek H, Rivet E, Laurence T, Fleury R. Toward wideband steerable acoustic metasurfaces with arrays of active electroacoustic resonators. *Int J Appl Phys* 2018;123:091714.
- [15] Aurégan Y, Farooqui M. In-parallel resonators to increase the absorption of subwavelength acoustic absorbers in the mid-frequency range. *Sci Rep* 2019;9:1–6.
- [16] C. Parente, N. Arcas, B. Walker, A. Hersh, E. Rice, Hybrid active/passive jet engine noise suppression system (1999).
- [17] Olson HF, May EG. Electronic sound absorber. *J Acoust* 1953;25:1130–6.
- [18] Guicking D, Lorenz E. An active sound absorber with porous plate (1984).
- [19] Furstoss M, Thenail D, Galland M-A. Surface impedance control for sound absorption: direct and hybrid passive/active strategies. *J Sound Vib* 1997;203:219–36.
- [20] Galland M-A, Mazeaud B, Sellen N. Hybrid passive/active absorbers for flow ducts. *Appl Acoust* 2005;66:691–708.
- [21] Lissek H. Shunt loudspeaker technique for use as acoustic liner. In: Proceedings of the Internoise 2009: Innovations in Practical Noise Control. p. 1–8.
- [22] Boulandet R, Lissek H. Optimization of electroacoustic absorbers by means of designed experiments. *Appl Acoust* 2010;71:830–42.
- [23] Lissek H, Boulandet R, Fleury R. Electroacoustic absorbers: bridging the gap between shunt loudspeakers and active sound absorption. *J Acoust* 2011;129:2968–78.
- [24] Boulandet R, Lissek H. Toward broadband electroacoustic resonators through optimized feedback control strategies. *J Sound Vib* 2014;333:4810–25.
- [25] Boulandet R, Rivet E, Lissek H. Sensorless electroacoustic absorbers through synthesized impedance control for damping low-frequency modes in cavities. *Acta Acust* 2016;102:696–704.
- [26] Bao J, Lee PL. Process control: the passive systems approach. Springer Science & Business Media; 2007.
- [27] Rivet E, Karkar S, Lissek H. Broadband low-frequency electroacoustic absorbers through hybrid sensor-/shunt-based impedance control. *IEEE T Contr Syst T* 2016;25:63–72.
- [28] Boulandet R, Lissek H, Karkar S, Collet M, Matten G, Ouisse M, Versaevel M. Duct modes damping through an adjustable electroacoustic liner under grazing incidence. *J Sound Vib* 2018;426:19–33.
- [29] De Bono E. Electro-active boundary control for noise mitigation: Local and Advective strategies, Ph.D. thesis, Université de Lyon, 2021.
- [30] Rienstra SW, Darau M. Boundary-layer thickness effects of the hydrodynamic instability along an impedance wall. *J Fluid Mecha* 2011;671:559.
- [31] Collet M, David P, Berthillier M. Active acoustical impedance using distributed electrodynamic transducers. *J Acoust* 2009;125:882–94.
- [32] Karkar S, De Bono E, Collet M, Matten G, Ouisse M, Rivet E. Broadband nonreciprocal acoustic propagation using programmable boundary conditions: From analytical modeling to experimental implementation. *Phys Rev Appl* 2019;12:054033.
- [33] Bolton JS, Yoo T, Olivieri O. Measurement of normal incidence transmission loss and other acoustical properties of materials placed in a standing wave tube. *Brüel & Kjær Technical Review* 2007:1–44.